

Optical properties of the spin-ladder compound $\text{Sr}_{14}\text{Cu}_{24}\text{O}_{41}$

Z. V. Popović,^{1,*} M. J. Konstantinović,^{2,†} V. A. Ivanov,^{1,‡} O. P. Khuong,^{1,§} R. Gajić,³ A. Vietkin,⁴ and V. V. Moshchalkov¹

¹Laboratorium voor Vaste-Stoffysica en Magnetisme, K. U. Leuven, Celestijnenlaan 200D, B-3001 Leuven, Belgium

²Max-Planck-Institut für Festkörperforschung, Heisenbergstrasse 1, D-70569 Stuttgart, Germany

³Institute of Physics, P.O. Box 68, 11080 Belgrade, Yugoslavia

⁴Physics Department, Moscow State University, 119899 Moscow, Russia

(Received 4 November 1999; revised manuscript received 3 March 2000)

We report the measurements of the pseudodielectric function, far-infrared reflectivity, and Raman scattering spectra in $\text{Sr}_{14}\text{Cu}_{24}\text{O}_{41}$ single crystal. We study the lattice and the spin dynamics of the Cu_2O_3 spin ladders and CuO_2 chains of this compound. The ellipsometric and the optical reflectivity measurements yield the gap values of 1.4, 1.86, 2.34 eV (2.5 eV) for the ladders (chains) along the c axis and 2.4 eV along the a axis. The electronic structure of the Cu_2O_3 ladders is analyzed using the tight-binding approach for the correlated electron systems. The correlation gap value of 1.4 eV is calculated with the transfer energy (hopping) parameters $t = t_0 = 0.26$ eV, along and perpendicular to legs, $t_{xy} = 0.026$ eV (interladder hopping) and $U = 2.1$ eV, as a Coulomb repulsion. The optical parameters of the infrared-active phonons and plasmons are obtained by an oscillator fitting procedure of the reflectivity spectra. Raman scattering spectra are measured at different temperatures using different laser line energies. The two-magnon peak is observed at about 2880 cm^{-1} . At temperatures below 150 K the new infrared and Raman modes appear due to the charge ordering.

I. INTRODUCTION

The $\text{Sr}_{14}\text{Cu}_{24}\text{O}_{41}$ compound is one of the three stable phases in the Sr-Cu-O system that can be synthesized under ambient pressure. The other two stable phases are Sr_2CuO_3 , which has simple chains of Cu ions, and SrCuO_2 with zigzag chains of Cu ions. This oxide has unique crystal structure based on two sublattices; one of them consists of Cu_2O_3 two-leg ladders and the second one is formed by CuO_2 chains. These two sublattices are incompatible along one crystallographic direction, thus resulting in a one-dimensional (1D) incommensurate structure.¹ According to the structural analysis,¹ the ladder sublattice is face-centered orthorhombic (space group $Fmmm$) with a lattice parameters $a = 1.1459$ nm, $b = 1.3368$ nm, and $c_{\text{Ladder}} = 0.3931$ nm. There are two ladder layers with two ladders per unit cell, Fig. 1. The chain sublattice is A-centered orthorhombic (space group $Amma$), with nearly the same a and b axes but different c axis, $c_{\text{Chain}} = 0.2749$ nm. However, $\text{Sr}_{14}\text{Cu}_{24}\text{O}_{41}$ can be considered as a nearly commensurate structure at $7c_{\text{Ladder}} = 2.7372$ nm and $10c_{\text{Chain}} = 2.7534$ nm. The schematic illustration of $\text{Sr}_{14}\text{Cu}_{24}\text{O}_{41}$ crystal structure is given in Fig. 1.

The physical properties of $\text{Sr}_{14}\text{Cu}_{24}\text{O}_{41}$ have attracted a lot of attention recently,²⁻¹² in connection with the rich physics associated with the $S = \frac{1}{2}$ Heisenberg antiferromagnetic quasi-1D structures and the discovery of superconductivity in $\text{Sr}_{0.4}\text{Ca}_{13.6}\text{Cu}_{24}\text{O}_{41}$ under high pressure.² The progress in this field has been summarized in Ref. 13. Various magnetic,³⁻⁵ NMR,^{6,7} and neutron scattering^{8,9} measurements showed that $\text{Sr}_{14}\text{Cu}_{24}\text{O}_{41}$ has two kinds of magnetic gaps. The first one, $\Delta_L = 32.5$ meV, is attributed to the singlet-triplet excitation in the Cu_2O_3 spin ladders, with the exchange energies along the legs ($J = 130$ meV) and the rungs ($J_0 = 72$ meV).⁸ The second one, $\Delta_C = 11.5$ meV, is

argued to arise from the spin dimer formation in the CuO_2 chains,⁸ with an antiferromagnetic intradimer coupling $J_1 = 11.2$ meV. A similar ratio of the superexchange interaction energies, $J_0/J \sim 0.5$, as well as the magnitude of $J_0 = 950 \pm 300$ K, is found in the ¹⁷O and ⁶³Cu NMR measurements.⁶

The Raman spectra of $\text{Sr}_{14}\text{Cu}_{24}\text{O}_{41}$ were measured previously.^{14,15} From a comparison between Raman spectra of the various layered tetragonal cuprates, Abrashev, Thomsen, and Surtchev¹⁴ concluded that the main contribution to the spectra comes from the Raman-forbidden infrared-active LO phonons and the two-magnon scattering. Furthermore, Sugai and Suzuki¹⁵ argued that, besides strong two-magnon features, some low-frequency modes in the Raman spectra are also magnetic in origin, since they have similar energies to those found in the neutron scattering experiments.⁸ Still, for the proper identification of the magnetic modes, the temperature-dependent Raman spectra as well as the spectra in magnetic field are required. Also, detailed analysis of the lattice dynamics and comparison between Raman and infrared (IR) spectra are indispensable due to the incommensurability of the structure. Therefore, we present here the Raman and IR spectra at various temperatures between 5 and 300 K in order to make more complete assignment of the vibrational modes in $\text{Sr}_{14}\text{Cu}_{24}\text{O}_{41}$. The Raman spectra are also measured under resonant conditions with a laser light energy close to gap values. The correlated electron tight-binding model of the electronic structure is used to estimate the hopping parameters, in fact, adjusted to the measured gaps and exchange energies.

II. EXPERIMENTAL DETAILS

The present work was performed on (010)-oriented single-crystal plates with dimensions typically about $5 \times 1 \times 6 \text{ mm}^3$ in the a , b , and c axes, respectively. The infrared measurements were carried out with a BOMEM DA-8 FIR

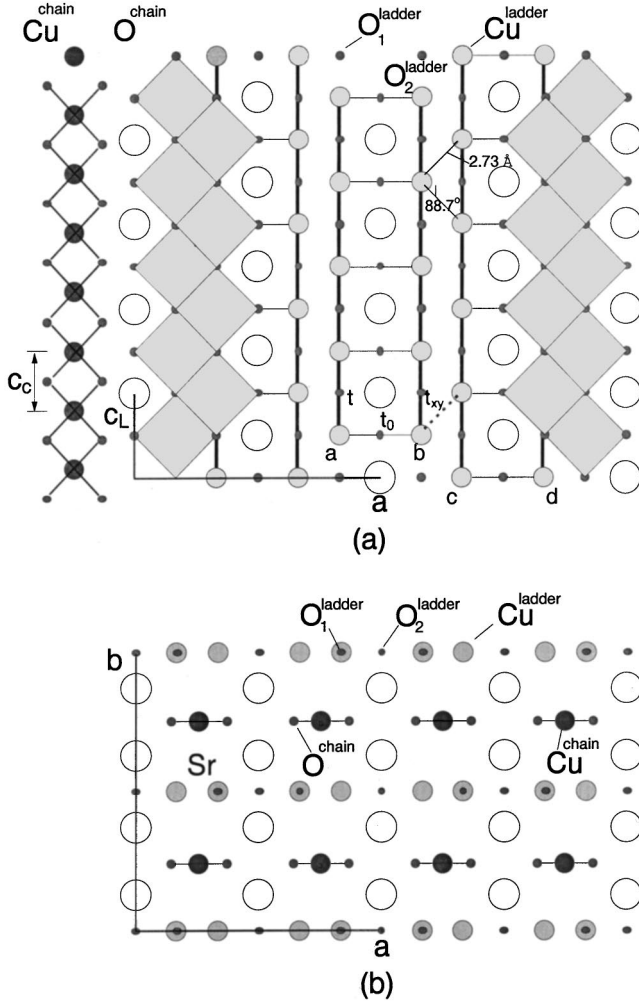


FIG. 1. Schematic representation of the $\text{Sr}_{14}\text{Cu}_{24}\text{O}_{41}$ crystal structure in the (a) (010) and (b) (001) plane.

spectrometer. A DTGS pyroelectric detector was used to cover the wave number region from 100 to 700 cm^{-1} ; a liquid-nitrogen-cooled $\text{Hg}_x\text{Cd}_{1-x}\text{Te}$ detector was used from 500 to 1500 cm^{-1} . The spectra were collected with 2-cm^{-1} resolution. The low-temperature reflectivity spectra in the range from 30 to 5000 cm^{-1} were measured using Bruker IFS 133v FIR spectrometer with the Oxford-Cryostat. The Raman spectra were recorded in the backscattering configuration using micro- and macro-Raman systems with Dilor triple monochromator including a liquid-nitrogen-cooled charge-coupled device detector. Ar- and Kr-ion lasers were used as an excitation source. We measured the pseudodielectric function with the help of a rotating analyzer ellipsometer. We used a Xe lamp as a light source, a double monochromator with 1200 lines/mm gratings, and an S20 photomultiplier tube as a detector. The polarizer and analyzer were Rochon prisms. The measurements were performed in the 1.6–5.6-eV energy range. Optical reflectivity spectra were measured at room temperature in the 200–2000-nm spectral range using a Perkin-Elmer Lambda 19 spectrophotometer.

III. ELECTRONIC STRUCTURE

The electronic structure of $\text{Sr}_{14}\text{Cu}_{24}\text{O}_{41}$ is calculated using the tight-binding method for correlated electrons.¹⁶ Recent

exact diagonalization and a variational Monte Carlo simulation revealed that electronic structure of $\text{Sr}_{14}\text{Cu}_{24}\text{O}_{41}$ is well described by single ladder energy spectrum.¹⁷ It means that electron energy dispersions are governed mainly by electrons in the ladder. According to the angle-resolved photoelectron spectroscopy measurements,¹⁰ the chains contribute to the electronic structure of $\text{Sr}_{14}\text{Cu}_{24}\text{O}_{41}$ with a dispersionless band. Without entering any lengthy discussions about the substance nonstoichiometry and the carrier transport between chains and ladders, we assume further that the ladder unit $\text{Cu}_2^{1+n}\text{O}_3^{2-}$ has total charge of -2 . In other words, there is one hole, $n=1$, per copper ion in the ladder for negligibly small hybridization of its $d_{x^2-y^2}$ orbitals with the p_y orbital of intermediate oxygens. The angle between Cu atoms of neighboring ladders is nearly right angle (88.7°), Fig. 1. In our consideration of the electronic structure we assumed that the directions between the nearest-neighbor Cu ions form an ideal right angle.

The Hamiltonian for the correlated copper holes in the ladder with two rungs, a - b and c - d , per a unit cell can be written as

$$\begin{aligned}
 H = & -2t \sum_{p,\sigma} \cos p_y [a_\sigma^+(p) a_\sigma(p) + b_\sigma^+(p) b_\sigma(p)] \\
 & + c_\sigma^+(p) c_\sigma(p) + d_\sigma^+(p) d_\sigma(p) - t_0 \sum_{p,\sigma} [a_\sigma^+(p) b_\sigma(p) \\
 & + c_\sigma^+(p) d_\sigma(p) + \text{H.c.}] - t_{xy} \sum_{p,\sigma} [e^{-i\sqrt{2}p_x} + e^{-i(\sqrt{2}p_x + p_y)}] \\
 & \times [a_\sigma^+(p) d_\sigma(p) + \text{H.c.}] - t_{xy} \sum_{p,\sigma} (1 + e^{-ip_y}) \\
 & \times [b_\sigma^+(p) c_\sigma(p) + \text{H.c.}] + U \sum_{i=a,b,c,d} n_{\uparrow i}^j n_{\downarrow i}^j \\
 & - \mu \sum_{i=a,b,c,d} n_i^j, \tag{1}
 \end{aligned}$$

where a, b, c, d represent chains [see Fig. 1(a)], $t(t_0)$ are the values of the carrier hopping along legs (rungs), t_{xy} is a hopping amplitude between ladders, U is the Anderson-Hubbard repulsion, μ is the chemical potential, and other notations are as usual. The x and y axes of the reference system are taken along the a and the c crystallographic directions, respectively. Applying the X -operator machinery,¹⁸ the correlation split energy bands are governed by zeros of the inverse Green's function in the first perturbation order with respect to tunneling matrix:

$$\hat{D}_p^{-1}(\omega) = \begin{pmatrix} A_{a-b} & B \\ B^* & A_{c-d} \end{pmatrix}, \tag{2}$$

where

$$\hat{A}_{a-b} = \begin{pmatrix} a \left\{ \begin{array}{cccc} 0+ & \frac{-i\omega_n - \mu}{f_{0+}} + r & r & -t_0 & -t_0 \\ -2 & r & \frac{-i\omega_n - \mu + U}{f_{-2}} + r & -t_0 & -t_0 \end{array} \right. \\ b \left\{ \begin{array}{cccc} 0+ & -t_0 & -t_0 & \frac{-i\omega_n - \mu}{f_{0+}} + r & r \\ -2 & -t_0 & -t_0 & r & \frac{-i\omega_n - \mu + U}{f_{-2}} + r \end{array} \right. \end{pmatrix},$$

$$\hat{B} = \begin{pmatrix} 0 & 0 & D & D \\ 0 & 0 & D & D \\ C & C & 0 & 0 \\ C & C & 0 & 0 \end{pmatrix}$$

with $r = -2t \cos p_y$, $C = -t_{xy}(1 + e^{-ip_y})$, $D = -t_{xy}[e^{-i\sqrt{2}p_x} + e^{-i(\sqrt{2}p_x + p_y)}]$.

Here the correlation factors f_{0+}, f_{-2} are determined by the fermion occupation n per site. For the considered paramagnetic phase they are $f_{0+} = 1 - n/2$, $f_{-2} = n/2$ and all equal to $\frac{1}{2}$ ($n=1$). After an analytical continuation, $i\omega_n \rightarrow \xi + i\delta$, in $|\hat{D}_p^{-1}(\omega)|=0$ one can find the bonding/antibonding correlation energy dispersions as follows:

$$\xi_B^\pm(p) = \frac{1}{2}[\varepsilon_p^{1,2} + \sqrt{(\varepsilon_p^{1,2})^2 + U^2}], \quad (3)$$

$$\xi_A^\pm(p) = \frac{1}{2}[\varepsilon_p^{1,2} - \sqrt{(\varepsilon_p^{1,2})^2 + U^2}], \quad (4)$$

where

$$\varepsilon_p^{1,2} = -2t \cos p_y \pm \sqrt{t_0^2 + (2t_{xy} \cos p_y/2)^2 \pm 4t_0 t_{xy} \cos p_y/2 \cos \sqrt{2}p_x/2}.$$

For derivation of these energy dispersions from the eight-by-eight-fold secular equation [see Eq. (2)] it was useful to apply the theorem about the decomposition of the determinant with respect to diagonal elements (see Appendix A in Ref. 19). The subbands ξ_B^- and ξ_A^- are completely occupied by carriers with concentration $n=1$ per copper site of ladder for the chosen chemical potential $\mu = U/2$. The nearest unoccupied energy band is ξ_B^+ and the correlation gap in the electronic structure can be estimated as

$$\Delta_{\text{corr}} = \min \xi_B^+(p) - \max \xi_A^-(p) = \frac{1}{2}[\sqrt{(t_0 + 2t - 2t_{xy})^2 + U^2} + \sqrt{(t_0 + 2t)^2 + U^2}] - (t_0 + 2t + t_{xy}). \quad (5)$$

For the dimensionless energies, $\omega_p^{+,-} = \varepsilon_p^{1,2}/2t$, $\tau_0 = t_0/2t$, $\tau = t_{xy}/2t$, the noncorrelated electron density of states per spin, $\rho(\varepsilon) = \sum_{p_x, p_y} [\delta(\varepsilon - \omega_p^+) + \delta(\varepsilon - \omega_p^-)]$, for the unit cell volume is defined analytically as follows:

$$\rho_0^\alpha(-1 - 2\tau + \alpha\tau_0 \leq \varepsilon \leq -1 + 2\tau - \tau_0) = \frac{4}{\pi^2 \sqrt{k_\alpha \tau}} K(q_\alpha),$$

$$\rho_0^\alpha(-1 + 2\tau + \alpha\tau_0 \leq \varepsilon \leq \frac{1}{2} + \tau + \alpha\tau_0) = \frac{4}{\pi^2 q_\alpha \sqrt{k_\alpha \tau}} F\left(\arcsin a_\alpha; \frac{1}{q_\alpha}\right), \quad (6)$$

$$\rho_0^\alpha(-1 + 2\tau + \alpha\tau_0 \leq \varepsilon \leq 1 + \alpha\tau_0) = \frac{4}{\pi^2 q_\alpha \sqrt{k_\alpha \tau}} K\left(\frac{1}{q_\alpha}\right).$$

Equations (6) represent the analytical expressions for the electron density of states via elliptic integrals F and K of the first kind in the Legendre normal form with modulus

$$q_\alpha = \sqrt{[2\tau(\tau + k_\alpha) + 1 - (\varepsilon + \alpha\tau_0)^2]/k_\alpha \tau/2},$$

and argument

$$a_\alpha = \sqrt{[2\tau(\tau + k_\alpha) + 1 - (\varepsilon + \alpha\tau_0)^2]/[(1 + \varepsilon + \alpha\tau_0)(\tau + k_\alpha)k_\alpha]},$$

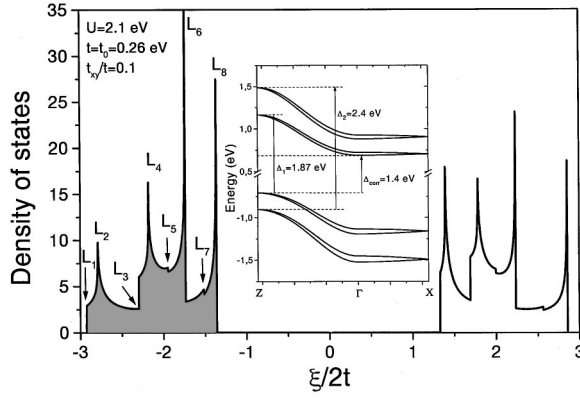


FIG. 2. The electron density of states as a function of dimensionless energies $\xi/2t$. Inset: The tight-binding dispersions for correlated electrons in $\text{Sr}_{14}\text{Cu}_{24}\text{O}_{41}$ with parameters $t=t_0=0.26$ eV, $t_{xy}=0.026$ eV. The momenta are given in units $|p_x\sqrt{2}|=|p_z|=\pi$ of the Brillouin zone boundaries, the Fermi energy $E_F=0$ is inside of the correlation gap.

where $k_\alpha = \sqrt{\tau^2 + 2(1 - \varepsilon - \alpha\tau_0)}$ and $\alpha = \pm$.

The electron-electron repulsion U splits the density of the noncorrelated electronic states ρ_0 . The correlated electron density of states is

$$\rho(\varepsilon) = \frac{2}{1 + \frac{\xi'_+}{\sqrt{(\xi'_+)^2 + \left(\frac{U}{2t}\right)^2}}} \rho_0(\xi'_+) + \frac{2}{1 - \frac{\xi'_-}{\sqrt{(\xi'_-)^2 + \left(\frac{U}{2t}\right)^2}}} \rho_0(\xi'_-), \quad (7)$$

where

$$\xi'_\pm = \frac{\xi_\pm^2 - \left(\frac{U}{2t}\right)^2}{\xi_\pm} + S$$

and

$$S = \frac{1}{4} \left[\sqrt{(1 + 2\tau + \tau_0)^2 + \left(\frac{U}{t}\right)^2} - \sqrt{(1 + \tau_0)^2 + \left(\frac{U}{t}\right)^2} - 2\tau \right],$$

are expressed via dimensionless correlated energies $\xi_\pm \equiv \xi^\pm(p)/2t$. With the help of Eqs. (7) and (6) one can calculate the correlated electron density of states for corresponding energy ranges. Its explicit form naturally includes the first kind of elliptic integrals. The results of the calculations are plotted in Fig. 2.

The overlap of the energy ranges for the electronic dispersions, Eq. (3), leads to the special features of the correlated electronic structure at

$$L_5 = 1/2(-1 - 2\tau + \tau_0) - S - 1/2\sqrt{(1 + 2\tau + \tau_0)^2 + (U/t)^2}$$

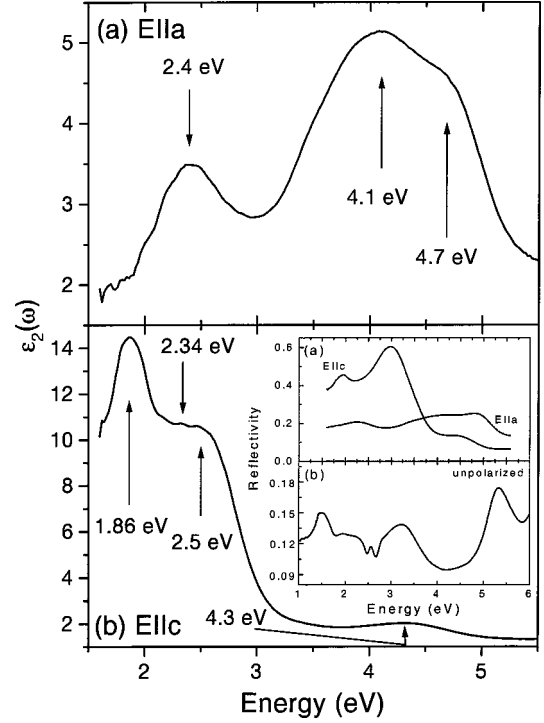


FIG. 3. Room-temperature imaginary part (ε_2) of the pseudodielectric function of $\text{Sr}_{14}\text{Cu}_{24}\text{O}_{41}$. The spectra of the (010) surface taken with (a) a axis, (b) c axis, parallel to the plane of incidence. Inset: (a) Reflectivity spectra obtained by calculation using ε_1 and ε_2 ; (b) unpolarized reflectivity spectrum measured at room temperature.

and

$$L_7 = 1/2(\frac{1}{2} + \tau + \tau_0) - S - 1/2\sqrt{(\frac{1}{2} + \tau + \tau_0)^2 + (U/t)^2}$$

in the lower correlated band. Logarithmic divergencies inside the band at

$$L_2 = 1/2(-1 + 2\tau - \tau_0) - S - 1/2\sqrt{(-1 + 2\tau - \tau_0)^2 + (U/t)^2},$$

$$L_4 = 1/2(1 - \tau_0) - S - 1/2\sqrt{(1 - \tau_0)^2 + (U/t)^2},$$

$$L_6 = 1/2(-1 + 2\tau + \tau_0) - S - 1/2\sqrt{(-1 + 2\tau + \tau_0)^2 + (U/t)^2}$$

and at the correlated band edge

$$L_8 = 1/2(1 + \tau_0) - S - 1/2\sqrt{(1 + \tau_0)^2 + (U/t)^2}$$

are clear manifestations of the 2D electronic structure of the $\text{Sr}_{14}\text{Cu}_{24}\text{O}_{41}$ compound. We would like to emphasize that in the one-dimensional case ($t_{xy} \rightarrow 0$) the electron density of states is taking features of a single spin ladder without any logarithmic peaks; then the divergencies become square-root-like and they are located at the band edges, $\varepsilon = \pm 1$: $\rho(\varepsilon) = 8K(0)/\pi^2\sqrt{1 - \varepsilon^2} = 4/\pi\sqrt{1 - \varepsilon^2}$.

IV. EXPERIMENTAL RESULTS

The dielectric function ε_2 of $\text{Sr}_{14}\text{Cu}_{24}\text{O}_{41}$ is shown in Fig. 3 in the spectral region from 1.6 to 5.5 eV. These spectra were computed from the measured Fourier coefficients using the equations for an isotropic case. Consequently, ε_2 represents a complicated average of the projections of the dielec-

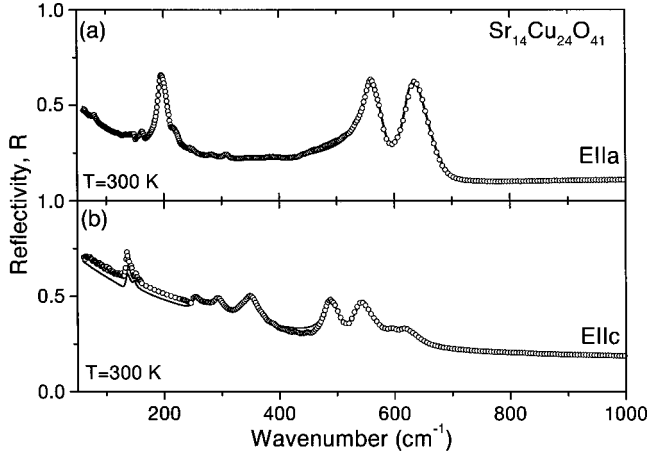


FIG. 4. Room-temperature polarized far-infrared reflectivity spectra of $\text{Sr}_{14}\text{Cu}_{24}\text{O}_{41}$ single crystal for (a) the $\mathbf{E}\parallel\mathbf{a}$ and (b) the $\mathbf{E}\parallel\mathbf{c}$ polarizations. The experimental values are given by the open circles. The solid lines represent the calculated spectra obtained by the fitting procedure described in the text.

tric tensor on the sample surface. We presented the spectra of the (010) surface taken with the a axis, Fig. 3(a), and c axis, Fig. 3(b), in the plane of incidence (PI). According to the prescription given by Aspnes,²⁰ we attribute these components to the components of the dielectric tensor ϵ_2^{aa} and ϵ_2^{cc} . The bands with the energies of 2.4, 4.1, and 4.7 eV for the a axis and at about 1.86, 2.34, 2.5, and 4.3 eV are found for the c axis in the plane of incidence, respectively.

Inset (a) in Fig. 3 shows reflectivity spectra of $\text{Sr}_{14}\text{Cu}_{24}\text{O}_{41}$. These spectra are calculated from measured dielectric functions ϵ_1 and ϵ_2 . Inset (b) in Fig. 3 represents the unpolarized optical reflectivity of $\text{Sr}_{14}\text{Cu}_{24}\text{O}_{41}$ measured at room temperature. In addition to peaks, previously observed in ellipsometric measurements, a new peak at about 1.4 eV appears.

The room-temperature polarized far-infrared reflectivity spectra of $\text{Sr}_{14}\text{Cu}_{24}\text{O}_{41}$ are given in Fig. 4. The open circles are the experimental data and the solid lines represent the spectra computed using a four-parameter model for the dielectric constant:

$$\epsilon(\omega) = \epsilon_\infty \left(\prod_{j=1}^n \frac{\omega_{\text{LO},j}^2 - \omega^2 + i\gamma_{\text{LO},j}\omega}{\omega_{\text{TO},j}^2 - \omega^2 + i\gamma_{\text{TO},j}\omega} - \frac{\omega_p^2}{\omega(\omega - i\tau^{-1})} \right), \quad (8)$$

where $\omega_{\text{LO},j}$ and $\omega_{\text{TO},j}$ are longitudinal and transverse frequencies of the j th oscillator, $\gamma_{\text{LO},j}$ and $\gamma_{\text{TO},j}$ are their corresponding dampings, ω_p is the plasma frequency, τ is the free-carrier relaxation time, and ϵ_∞ is the high-frequency dielectric constant.

The best fit parameters are given in Table I. The agreement between the observed and calculated reflectivity spectra is rather good. For the $\mathbf{E}\parallel\mathbf{a}$ polarization, eight oscillators with TO frequencies at about 164, 194, 219, 249, 283.5, 310.4, 554, and 623 cm^{-1} are clearly seen. In the $\mathbf{E}\parallel\mathbf{c}$ polarization, Fig. 4(b), nine oscillators at 135, 148, 253, 293, 345, 486, 540, 596, and 620 cm^{-1} are observed. Besides phonons, our model includes the Drude expression for light scattering on free carriers. We obtained the plasma frequency at about 4000 cm^{-1} (1000 cm^{-1}) for the $\mathbf{E}\parallel\mathbf{c}$ ($\mathbf{E}\parallel\mathbf{a}$) polarizations.

TABLE I. Oscillator fit parameters (in cm^{-1}) of the reflectivity data, $T = 300$ K.

Polarization	ω_{TO}	γ_{TO}	ω_{LO}	γ_{LO}	ω_p	τ^{-1}	ϵ_∞
$\mathbf{E}\parallel\mathbf{a}$	164	6	164.6	5.5			
	194	6	210	14			
	219	10	223	10			
	249	14	250	14			
	283.5	14	284	14	1000	4000	4.8
	310.4	8	311	8			
	554	16	585	28			
	623	19	676	22			
$\mathbf{E}\parallel\mathbf{c}$	135	6	140	10			
	148	5	150	5			
	253	12	257	17			
	293	18	300	14			
	345	26	364	10	4000	18200	4
	486	20	502	20			
	540	25	568	17			
	596	20	600	17			
	620	30	629	14			

The room-temperature Raman spectra of $\text{Sr}_{14}\text{Cu}_{24}\text{O}_{41}$, for (aa) and (cc) polarized configurations are presented in Figs. 5(a) and 5(b). These spectra consist of only A_g symmetry modes. Four modes at 246, 302, 548, and 582 cm^{-1} are clearly seen. The low temperature (cc) Raman spectra are given in Figs. 5(c)–5(g). By lowering the temperature below 200 K, the modes narrow and in addition the new modes appear. We will discuss them later on. The Raman spectra of $\text{Sr}_{14}\text{Cu}_{24}\text{O}_{41}$, excited by different lines of Ar and Kr lasers at 8 K, are shown in Fig. 6 for the (cc) and (aa) polarized

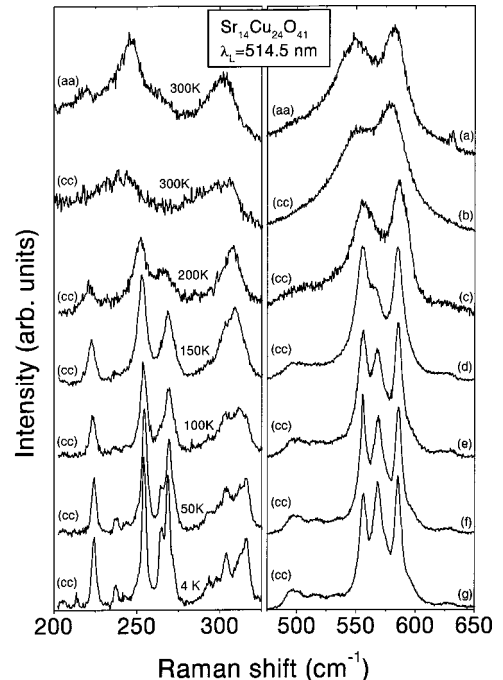


FIG. 5. Temperature-dependent Raman scattering spectra for (aa) polarized (a) and (cc) polarized (b)–(g) configurations. $\lambda_L = 514.5$ nm.

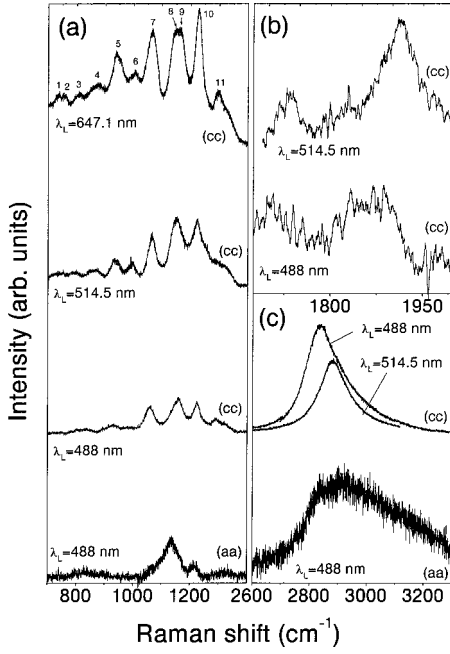


FIG. 6. Raman spectra measured at $T=8$ K in the 700–3300- cm^{-1} spectral range.

configurations in the spectral ranges: (a) from 700 to 1400 cm^{-1} , (b) from 1675 to 1975 cm^{-1} , and (c) from 2600 to 3300 cm^{-1} . Anticipating our conclusions, we divide the Raman spectra in three different energy regions: one-phonon (0–700 cm^{-1}), two-phonon (700–1400 cm^{-1}), and two-magnon region (above 1500 cm^{-1}). The mode at about 2900 cm^{-1} and a broad structure at about 1900 cm^{-1} are magnetic in origin, according to their intensity and frequency dependence as a function of the temperature, see Fig. 7.

V. DISCUSSION

The average unit cell of $\text{Sr}_{14}\text{Cu}_{24}\text{O}_{41}$ consists of four formula units with 316 atoms in all. Since there is a large num-

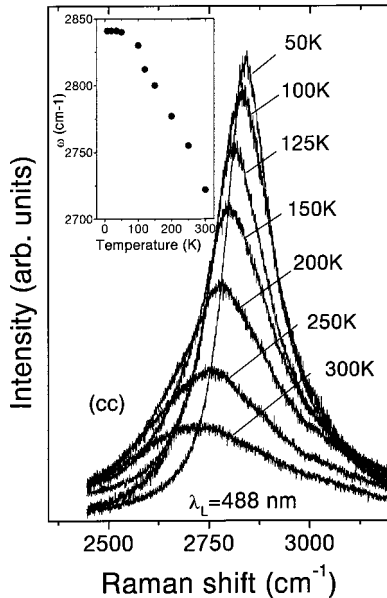


FIG. 7. Frequency and intensity dependencies of the two-magnon mode at about 2840 cm^{-1} as a function of temperature.

ber of atoms in the unit cell, we can expect a very large number of optically active modes. Consequently, the lattice dynamical calculation is practically impossible. All atoms have 4(*e*) position symmetry of $Pcc2$ (C_{2v}^3) space group.¹ Factor-group-analysis (FGA) yields the following distribution of vibrational modes:

$$\Gamma_{\text{Sr}_{14}\text{Cu}_{24}\text{O}_{41}} = 237A_1(\mathbf{E}\parallel\mathbf{c},aa,bb,cc) + 237A_2(ab) + 237B_1(\mathbf{E}\parallel\mathbf{a},ac) + 237B_2(\mathbf{E}\parallel\mathbf{b},bc). \quad (9)$$

According to this representation one can expect 948 modes that are both Raman and infrared active. Experimentally, the number of observed modes is less than ten for each polarization. Because of that, we consider separately the contribution of each sublattice unit. As mentioned earlier, the space group of the ladder sublattice is $Fm\bar{m}n(D_{2h}^{23})$. The site symmetries of Sr, Cu, O₁, and O₂ atoms are (8*h*), (8*g*), (8*g*), and (4*b*), respectively. The FGA for the ladder structure ($\text{Sr}_2\text{Cu}_2\text{O}_3$) yields²¹

$$\Gamma_{\text{Ladder}} = 3A_g + 3B_{1g} + 2B_{2g} + B_{3g} + 4B_{1u} + 4B_{2u} + 4B_{3u}.$$

The space group of a chain sublattice is $Amma(D_{2h}^{17})$. The site symmetries of Cu and O atoms are (4*c*) and (8*f*). The FGA gives for the chain structure

$$\Gamma_{\text{Chain}} = 3A_g + 3B_{1g} + 2B_{2g} + B_{3g} + A_u + 2B_{1u} + 3B_{2u} + 3B_{3u}.$$

Since *Amma* is not a standard setting for D_{2h}^{17} space group (*Cmcm*) we use C_s^{xy} site symmetry for oxygen atoms and C_{2v}^x symmetry for Cu atoms in the above representations. Thus, the total number of vibrational modes from both sublattices is

$$\Gamma = 6A_g(aa,bb,cc) + 6B_{1g}(ab) + 4B_{2g}(ac) + 2B_{3g}(bc) + A_u + 6B_{1u}(\mathbf{E}\parallel\mathbf{c}) + 7B_{2u}(\mathbf{E}\parallel\mathbf{b}) + 7B_{3u}(\mathbf{E}\parallel\mathbf{a}). \quad (10)$$

According to this analysis we should expect 6 A_g modes; one mode from vibrations of the Sr atoms, two modes that originate from vibrations of Cu atoms, and the other three A_g modes are due to oxygen vibrations. In order to assign the observed A_g modes we compare our spectra with the corresponding spectra of the Cu-O based materials with similar structural units as in $\text{Sr}_{14}\text{Cu}_{24}\text{O}_{41}$. For example, in SrCuO_2 (Ref. 22) and $\text{YBa}_2\text{Cu}_4\text{O}_8$ (Ref. 23) the Cu-O double layers exist and resemble the one leg of the ladder structure in $\text{Sr}_{14}\text{Cu}_{24}\text{O}_{41}$. The Cu-O chains, formed from copper oxide squares with the common edges, as in $\text{Sr}_{14}\text{Cu}_{24}\text{O}_{41}$, are also present in CuO (Ref. 24) and CuGeO_3 .²⁵ Thus, the lowest-frequency mode in Fig. 5(a) at 246 cm^{-1} can be assigned to vibrations of the Cu ladder atoms (see Fig. 1). The corresponding A_g mode of copper vibrations in $\text{YBa}_2\text{Cu}_4\text{O}_8$ (SrCuO_2) appears at 250 (263) cm^{-1} . The next mode is found at 302 cm^{-1} . This mode represents the vibrations of the chain oxygen atoms along the *a* axis and appears in CuO at the same frequency.²⁴ The mode at 548 cm^{-1} is the breathing mode of O₁ oxygen ladder atoms. A similar mode appears in SrCuO_2 at 543 cm^{-1} . The second oxygen ladder atom (O₂), Fig. 1, is situated in the center of inversion

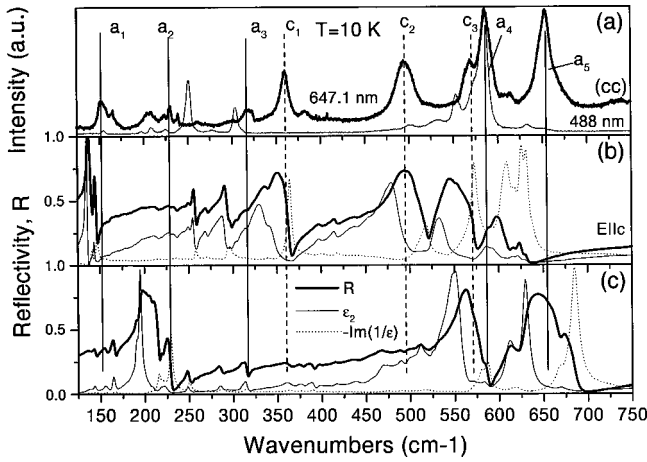


FIG. 8. (a) The (cc) polarized Raman spectra measured at $T = 10$ K with 647.1- and 488-nm excitation lines. (b) Polarized far-infrared reflectivity spectra measured at $T = 10$ K for $\mathbf{E}||c$ (b) and $\mathbf{E}||a$ (c) polarizations. Dielectric functions $\epsilon_2(\omega)$ and $-\text{Im}[1/\epsilon(\omega)]$ are obtained using KKA of reflectivity data.

(D_{2h} site symmetry) and has no Raman activity. The highest-frequency Raman mode in Figs. 5(a) and 5(b), at about 582 cm^{-1} , is caused by the chain oxygen vibrations along the c axis. A corresponding mode appears in CuO at 633 cm^{-1} (Ref. 24) and in CuGeO₃ at 594 cm^{-1} .²⁵ The vibrations of Sr atoms, with frequency of 188 cm^{-1} as in SrCuO₂, are not observed in the spectra. Finally, the A_g mode at 153 cm^{-1} , see Fig. 8, originates from the vibrations of the Cu atom in chains. Again, similar mode is found in YBa₂Cu₄O₈ at 153 cm^{-1} .

By lowering the temperature, Raman peaks narrow and at about $T = 150$ K the new modes appear (Fig. 5 and Table II). Similar effects are found in the IR spectra as well. This temperature coincides with the charge ordering temperature established in the NMR and neutron scattering experiments.^{7,9} NMR study⁷ showed the splitting of the signal from Cu³⁺ ions into two peaks below 200 K suggesting the occurrence of charge ordering. This effect is confirmed by Cox *et al.*¹¹ They measured synchrotron x-ray scattering on Sr₁₄Cu₂₄O₄₁ single crystals and showed the appearance of the satellite peaks at (001) positions. The results are interpreted in terms of a charge-ordered model involving both dimerization between two-nearest-neighbors of Cu²⁺ ions surrounding a Cu³⁺ ion on a Zhang-Rice singlet site, and dimerization between nearest neighbors of Cu²⁺ ions.

Figure 8(a) shows the (cc) polarized low temperature ($T = 10$ K) Raman spectra of Sr₁₄Cu₂₄O₄₁ in the 125–750-cm⁻¹ spectral region, excited with 647.1-nm (1.91 eV) and 488-nm (2.54 eV) energies. There is a remarkable difference between Raman spectra for these excitation lines that appears due to resonance effects. Namely, both lines are very close to gap energies for polarization along the c axis, see Fig. 3. The reflectivity spectra measured at 10 K for the E||c and the E||a polarizations are given in Figs. 8(b) and 8(c), respectively. In order to compare Raman with IR data we show in the same figure the $\epsilon_2(\omega)$ and the $-\text{Im}[1/\epsilon(\omega)]$ spectra. These spectra are obtained using Kramers-Kronig analysis of reflectivity data. The TO and LO mode frequencies are obtained as peak positions of the $\epsilon_2(\omega)$ and the $-\text{Im}[1/\epsilon(\omega)]$, respectively. For almost all Raman-active

TABLE II. Frequencies (in cm⁻¹) of Raman active modes measured at $T = 8$ K with $\lambda_L = 488, 514.5,$ and 647.1 nm, [Figs. 5(g) and 8(a)]. The asterisk denotes the modes influenced by charge ordering.

488 nm	514.5 nm	647.1 nm	Remark
		115	
154		153	a_1
197			
208	213*	208	a_2
224	224	223	
		230	
	237*	238	
251	254		
	265*		
	268*		
	293*		
304	304		
	316	316	a_3
		359	c_1
		381	
500	497*	496	c_2
	516*		
532	535*		
553	556		
	568*	568	c_3
586	585	585	a_4
632	630		
		652	a_5

modes we found their infrared counterparts (some of them are denoted by vertical lines) either for the E||a or the E||c polarizations. The appearance of similar lines in IR and Raman spectra, if not being the consequence of the symmetry, may also be attributed to the resonant conditions. It is well documented^{26,27} that Raman-forbidden IR-active LO modes appear in the Raman spectra of the insulating Cu-O based materials for the laser line energies close to gap values. The appearance of these modes in the Raman spectra is explained by Fröhlich interaction.²⁶ Here, since the 647.1-nm line is very close to the gap values (1.86 eV, see Fig. 3) one can expect that the IR LO modes appear in the Raman spectra of Sr₁₄Cu₂₄O₄₁ as well. Such an effect is usually accompanied by the observation of the strong phonon overtones, as we show in Fig. 6(a). All modes with energies higher than 700 cm^{-1} are in fact the second-order combinations (overtones) of the low-energy modes. The assignment and the frequencies of these modes are given in Table III. Therefore, the properties of the modes observed in our spectra may be understood in terms of the available symmetry combined with resonant effects, thus making proper identification of the low-temperature phonons practically impossible without detailed structural analysis.

Now we focus on magnetic properties. As was mentioned earlier, the neutron scattering and NMR measurements estimated the spin-ladder gap value to be at $\Delta_L = 32.5 \text{ meV}$ (268 cm^{-1}) (Ref. 8) or at 40.5 meV (326 cm^{-1}),²⁸ respectively. Because of that, we paid special attention to the 200–350-cm⁻¹ spectral range (Fig. 5 left panel). By lower-

TABLE III. Mode frequencies (in cm^{-1}) observed in Raman spectra measured with $\lambda_L = 647.1$ nm, Fig. 6(a).

No. of peaks	Frequency	Remark
1	735	$a_1 + a_4$
2	758	
3	805	$a_1 + a_5$
4	860	$a_2 + a_5$
5	946	$c_1 + a_4$
6	1005	$c_1 + a_5$
7	1069	$c_2 + c_3$
8	1152	$c_2 + a_5$
9	1164	$2a_4$
10	1132	$a_4 + a_5$
11	1300	$2a_5$

ing the temperature we observe the appearance of the new modes at 262, 293, and 317 cm^{-1} . At the same time we find the modes with the same energy in the low-temperature IR spectra, Figs. 8(b) and 8(c). The 262-cm^{-1} mode is very close in energy to the magnetic gap, thus possibly one-magnon excitation, as proposed by Sugai and Suzuki.¹⁵ However, the origin of the one-magnon excitation in the light scattering process usually comes from the spin-orbit interaction, which is found to be very small in transition-metal oxides due to quenched orbital momentum of the transition-metal ions. Moreover, below 100 K, this mode has nearly the same temperature dependency of the frequency and intensity, like all other low-temperature modes and we identify them as zone edge phonons, which become Raman active due to the zone-folding effect caused by the charge-ordering transition.⁷ Yet another type of magnetic excitation is expected to appear in the Raman spectra of two-leg ladders at energies close to $2\Delta_L \sim 534 \text{ cm}^{-1}$.²⁹ The mode at 498 cm^{-1} [see Fig. 5(g), right panel] shows a typical asymmetric shape with a tail towards high frequencies, as expected for the onset of the two-magnon continuum. Its energy difference from $2\Delta_L$ could be the magnon binding energy. However, as it is shown in Fig. 8(b), this mode is positioned between TO and LO frequencies of very strong IR active mode in the $\text{El}lc$ spectra. This mode also shows a strong resonant enhancement, see Fig. 8(a). Therefore, at this stage, it is hard to make definite conclusions about the origin of this mode and further experiments are needed to clarify this issue. Similar discussion holds for the spectral range around the twice the spin-gap value associated with chains, $2\Delta_C \sim 180 \text{ cm}^{-1}$, where a continuumlike feature is also found in the Raman spectra.

Finally, we discuss the modes in the spectral range above 1500 cm^{-1} . The strongest mode in the spectra is centered at about 2840 cm^{-1} for the 488-nm excitation and at about 2880 cm^{-1} for the 514.5-nm excitation line. This feature decreases in intensity and shifts to lower energies at higher temperatures, Fig. 7. The same structure is already observed in many copper oxides at similar frequencies.^{27,29} Thus, all observed effects indicate the two-magnon origin of this mode. The energy of the two-magnon mode, associated with a top of the magnon branch, in copper oxide insulators is about $3J$, where J represents the exchange interaction.

In the case of the two-leg ladders, its energy position for

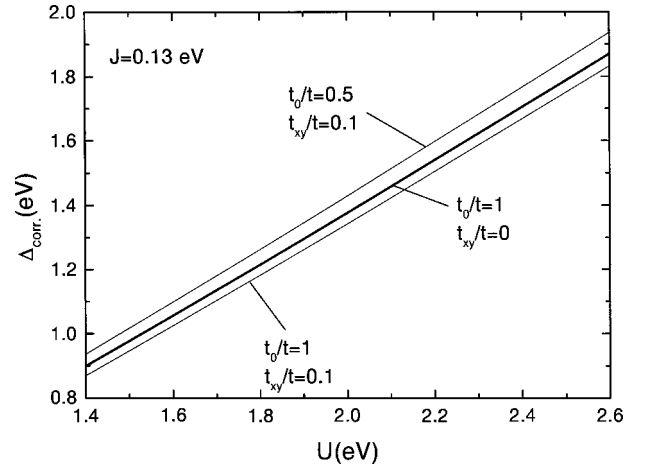


FIG. 9. The correlation gap vs U parameter dependence for different transfer energy ratios.

different polarized configurations in the Raman spectra may be used to estimate the exchange parameters parallel (J) and perpendicular (J_0) to the ladders.³⁰ Since the energy position of the two-magnon peak is the same for (cc) and (aa) polarizations, Fig. 6(c), such an analysis suggests that $J = J_0$. This conclusion is fully in agreement with Raman scattering data of Ref. 15 and recent high-energy neutron scattering measurements,³¹ but inconsistent with previous neutron,⁸ NMR,⁶ and magnetization measurements, which estimated the J_0/J ratio to be between 0.5 and 0.8. The discrepancy may be related to the fact that in the previous measurements, the high-energy magnetic excitations were not observed directly, but estimated indirectly from the low-energy spin gap measurements assuming an ideal model.³² Thus, the Raman scattering is a more direct method to obtain the J_0/J ratio. The two-magnon mode at 2880 cm^{-1} gives exchange energy $J = 119 \text{ meV}$, very close to the neutron scattering value $J = 130 \text{ meV}$.⁸

It is also interesting to note that the two-magnon mode is asymmetric with the spectral weight shifted to higher frequencies. Such a spectral shape of the two-magnon mode can be a consequence of the resonances,³³ or it can be related to the bound-hole-pair effects.¹⁵ Still, further experiments on the hole-doped crystals are necessary to clarify this point.

Let us consider Fig. 6(b), where a weak structure appears in (cc) spectra at about 1920 cm^{-1} . Its energy is exactly equal to $2J$ and varies with the laser line frequency in a similar way as the two-magnon mode at 2880 cm^{-1} . The energy shift of this mode as a function of temperature was not seen because of its very low intensity, thus leaving the origin of this mode as an open question. In addition to the 1920-cm^{-1} mode, we found a weak structure at about 1700 cm^{-1} , as well. This mode does not possess any noticeable temperature dependencies of energy and intensity. We concluded that this mode is an overtone phonon mode. Its frequency can be represented as the third order of the 568-cm^{-1} mode ($3c_3$, see Table II).

Finally, we discuss the electron energy dispersions and density of states, which are calculated using the model described in Sec. III. First, we analyze the influence of the energy transfer (hopping) to the correlation gap. Figure 9 shows the correlation gap Δ_{corr} vs the Anderson-Hubbard

parameter U . The plotted curves are calculated using Eq. (5) and $J=4t^2/U=0.13$ eV for different hopping energy ratios t_{xy}/t and t_0/t . From Fig. 9 we conclude that the main influence to the correlation gap value comes from the Anderson-Hubbard parameter U . Because of that, by knowing the electronic gap from the ellipsometric or optical absorption measurements and the exchange energy J from the Raman spectroscopy we can determine the hopping parameters and the on-site electron-electron repulsion U . However, the relative ratio of the hopping energies perpendicular and parallel to the legs as well as the interladder hopping does not influence much the correlation gap. Namely, a decrease of the transfer energy along the rungs from $t_0/t=1$ to $t_0/t=0.5$ increases Δ_{corr} by about 6%. Also, an increase of the interladder hopping t_{xy} from 0 to 10% of the hopping value t along the legs produces a decrease of Δ_{corr} of about 2.5%. Therefore, the interladder effects on electronic structure of $\text{Sr}_{14}\text{Cu}_{24}\text{O}_{41}$ are found to be negligibly small even though the distance between the neighboring ladders is short (see Fig. 1). The correlation gap is observed at 1.4 eV. This value is determined as the maximum of the dielectric function $\epsilon_2(\omega)$ obtained from Kramers-Kronig analysis of the unpolarized reflectivity data, see inset (b) of Fig. 3(b). Using this value and the fact that $t_0/t=1$ (comes from $J_0/J=1$), $t_{xy}=0$ we obtained $U=2.1$ eV. Similar values for the correlation gap and U have been also found in SrCuO_2 .³⁴

Energy dispersion, shown in the inset of Fig. 2, allows us to assign the 1.86-eV peak in Fig. 3(a) to the gap value ($\Delta_1=1.87$ eV) between bonding and antibonding bands at the Z point. Also, the 2.4-eV peak from the ellipsometric measurements corresponds to the gap from the lowest occupied band (L_6 , Fig. 2) to the highest empty band at the Z point of the Brillouine zone ($\Delta_2=2.4$ eV). By comparison of our measured and calculated gap values with previously published results,^{17,35} we found that our t_0/t ratio is close to the ratio determined in Ref. 17. Mizuno, Tahoyama, and

Maekawa³⁵ calculated the optical conductivity for small clusters, simulating the ladders and the chains. They obtained the gap for the ladder at about 1.7 eV while the contribution from the chains mainly emerges at a higher energy showing the large spectral weight at around 2.6 eV. These values are very close to our experimental results. Therefore, the peaks at 1.86, 2.4, and 2.5 eV, see Fig. 3(b), may correspond to the ladders and the chains, respectively.

In conclusion, we studied the optical properties of the $\text{Sr}_{14}\text{Cu}_{24}\text{O}_{41}$ single crystal. The lattice vibrations are analyzed using the far-infrared reflectivity and Raman scattering measurements in a wide frequency and temperature range. At temperatures below 150 K the new IR and Raman modes appear, presumably due to the charge ordering. The two-magnon excitations are found in the Raman spectra that could be related to minimal (2Δ) and maximal (twice the top of the magnon brunch) magnon energy. The exchange constants along the legs and rungs of the ladders are found to be the same, $J=J_0\sim 120$ meV. The optical reflectivity and the ellipsometric measurements are used to study the charge dynamics. The gap values of 1.4, 1.86 eV (2.5 eV) for the ladders (chains) along the c axis and 2.4 eV along the a axis are found. These results are analyzed using the tight-binding approach for the correlated electrons. The correlation gap value of 1.4 eV is calculated with the transfer energy (hopping) parameters $t=t_0=0.26$ eV along and perpendicular to the legs, and $U=2.1$ eV, as a Coulomb repulsion.

ACKNOWLEDGMENTS

We thank W. König for low-temperature infrared measurements. Z.V.P., V.A.I., and O.P.K. acknowledge support from the Research Council of the K.U. Leuven and DWTC. The work at the K.U. Leuven was supported by the Belgian IUAP and Flemish FWO and GOA Programs. M.J.K. thanks Roman Herzog–AvH for partial financial support.

*On leave from Institute of Physics, 11080 Belgrade, P.O. Box 68, Yugoslavia.

†Present address: Department of Physics, Simon Fraser University, 8888 University Drive, Burnaby, B.C., Canada, V5A 1S6.

‡On leave from N.S. Kurnakov Institute of the General and Inorganic Chemistry of the Russian Academy of Sciences, Leninskii Prospect 31, 117 907 Moscow.

§On leave from Institute of Engineering Physics, Hanoi University of Technology, 10 000 Hanoi, Vietnam.

¹E. M. McCarron, M. A. Subramanian, J. C. Calabrese, and R. L. Harlow, *Mater. Res. Bull.* **23**, 1355 (1988).

²M. Uehara, T. Nagata, J. Akimitsu, H. Takahashi, N. Mori, and K. Kinoshita, *J. Phys. Soc. Jpn.* **65**, 2764 (1996).

³N. Motoyama, T. Osafune, T. Kakeshita, H. Eisaki, and S. Uchida, *Phys. Rev. B* **55**, R3386 (1997).

⁴S. A. Carter, B. Batlogg, R. J. Cava, J. J. Krajewski, W. F. Peck, Jr., and T. M. Rice, *Phys. Rev. Lett.* **77**, 1378 (1996).

⁵Z. Hiroi, S. Amelinckx, G. Van Tendeloo, and N. Kobayashi, *Phys. Rev. B* **54**, 15 849 (1996).

⁶T. Imai, K. R. Thurber, K. M. Shen, A. W. Hunt, and F. C. Chou, *Phys. Rev. Lett.* **81**, 220 (1998).

⁷M. Takigawa, N. Motoyama, H. Eisaki, and S. Uchida, *Phys. Rev. B* **57**, 1124 (1998).

⁸R. S. Eccleston, M. Uehara, J. Akimitsu, H. Eisaki, N. Motoyama, and S. Uchida, *Phys. Rev. Lett.* **81**, 1702 (1998).

⁹M. Matsuda, K. Katsumata, H. Eisaki, N. Motoyama, S. Uchida, S. M. Shapiro, and G. Shirane, *Phys. Rev. B* **54**, 12 199 (1996).

¹⁰T. Takahashi, T. Yokoya, A. Ashihara, O. Akaki, H. Fujisawa, A. Chainani, M. Uehara, T. Nagata, J. Akimitsu, and H. Tsunetsuga, *Phys. Rev. B* **56**, 7870 (1997).

¹¹D. E. Cox, T. Iglesias, K. Hirota, G. Shirane, M. Matsuda, N. Motoyama, H. Eisaki, and S. Uchida, *Phys. Rev. B* **57**, 10 750 (1998).

¹²T. Osafune, N. Motoyama, H. Eisaki, and S. Uchida, *Phys. Rev. Lett.* **78**, 1980 (1997); B. Ruzicka, L. Degiorgi, U. Ammerahl, G. Dhalenne, and A. Revcolevschi, *Eur. Phys. J. B* **6**, 301 (1998).

¹³E. Dagotto, *Rep. Prog. Phys.* **62**, 1527 (1999).

¹⁴M. V. Abrashev, C. Thomsen, and M. Surtchev, *Physica C* **280**, 297 (1997).

¹⁵S. Sugai and M. Suzuki, *Phys. Status Solidi B* **215**, 653 (1999).

¹⁶V. A. Ivanov, *J. Phys.: Condens. Matter* **6**, 2065 (1994).

¹⁷S. Koike, K. Yamaji, and T. Yanagisawa, *J. Phys. Soc. Jpn.* **68**, 1657 (1999).

¹⁸V. A. Ivanov, *Physica B* **186-188**, 921 (1993).

¹⁹V. A. Ivanov, K. Yukushi, and E. Ugolkova, *Physica C* **275**, 26 (1997).

- ²⁰D. E. Aspnes, *J. Opt. Soc. Am.* **70**, 1275 (1980).
- ²¹D. L. Rousseau, R. P. Bauman, and S. P. S. Porto, *J. Raman Spectrosc.* **10**, 253 (1980).
- ²²M. V. Abrashev, A. P. Litvinchuk, C. Thomsen, and V. N. Popov, *Phys. Rev. B* **55**, 9136 (1997).
- ²³E. T. Hayen, R. Liu, C. Thomsen, R. Kremer, M. Cardona, J. Karpinski, E. Kaldis, and S. Rusiecki, *Phys. Rev. B* **41**, 11 058 (1990).
- ²⁴G. Kliche and Z. V. Popović, *Phys. Rev. B* **42**, 10 060 (1990).
- ²⁵Z. V. Popović, S. D. Dević, V. N. Popov, G. Dhalenne, and A. Revcolevschi, *Phys. Rev. B* **52**, 4185 (1995).
- ²⁶E. T. Heyen, J. Kircher, and M. Cardona, *Phys. Rev. B* **45**, 3037 (1992).
- ²⁷Y. Tokura, S. Koshihara, T. Arima, H. Takagi, S. Ishibashi, T. Ido, and S. Uchida, *Phys. Rev. B* **41**, 11 657 (1990).
- ²⁸S. Tsuji, K. Kumagai, M. Kato, and Y. Koike, *J. Phys. Soc. Jpn.* **65**, 3474 (1996).
- ²⁹M. J. Konstantinović, Z. V. Popović, M. Isobe, and Y. Ueda, *Phys. Rev. B* **61**, 15 185 (2000).
- ³⁰S. Sugai, T. Shinoda, N. Kobayashi, Z. Hiroi, and M. Takano, *Phys. Rev. B* **60**, R6969 (1999).
- ³¹M. Matsuda, K. Katsumata, R. S. Eccleston, S. Brehmer, and H. J. Mikeska, *J. Appl. Phys.* **87**, 6271 (2000), as discussed in Ref. 13.
- ³²T. Barnes, E. Dagotto, J. Riera, and E. S. Swanson, *Phys. Rev. B* **47**, 3196 (1993).
- ³³R. Liu, M. V. Klein, D. Salamon, S. L. Cooper, W. C. Lee, S. W. Cheong, and D. M. Ginsberg, *J. Phys. Chem. Solids* **54**, 1347 (1993).
- ³⁴Z. V. Popović, V. A. Ivanov, H. J. Konstantinovic, A. Cantarero, J. Martinez-Pastor, D. Olguin, M. I. Alonso, M. Garriga, O. P. Khuong, A. Vietkin, and V. V. Moshchalkov (unpublished).
- ³⁵Y. Mizuno, T. Tahoyama, and S. Maekawa, *J. Phys. Soc. Jpn.* **66**, 937 (1997).